JOURNAL OF AGRICULTURAL AND FOOD CHEMISTRY

Article

Cite This: J. Agric. Food Chem. 2018, 66, 10169−10178

pubs.acs.org/JAFC

Identification of Key Residues Associated with the Interaction between *Plutella xylostella* Sigma-Class Glutathione S-Transferase and the Inhibitor *S*-Hexyl Glutathione

Jiyuan Liu,[†,⊥] Yifan Li,[†,⊥] Zhen Tian,[‡,⊥] Hong Sun,[†] Xi'en Chen,[§] Shengli Zheng,[∥] and Yalin Zhang*[,†]

[†]Key Laboratory of Plant Protection Resources & Pest Management of the Ministry of Education, College of Plant Protection, Northwest A&F University, Yangling, Shaanxi 712100, China

[‡]College of Horticulture and Plant Protection, Yangzhou University, Wenhui East Road, Number 48, Yangzhou, Jiangsu 225009, China

[§]Department of Entomology, College of Agriculture, Food and Environment, University of Kentucky, Lexington, Kentucky 40546, United States

[∥]College of Chemistry & Pharmacy, Northwest A&F University, Number 3 Taicheng Road, Yangling, Shaanxi 712100, China

Supporting Information

ABSTRACT: Glutathione S-transferases (GSTs) are important detoxification enzymes involved in the development of metabolic resistance in *Plutella xylostella*. Uncovering the interactions between representative PxGSTs and the inhibitor *S*-hexyl glutathione (GTX), helps in the development of effective PxGST inhibitors for resistance management. As the PxGST most severely inhibited by GTX, PxGSTσ (sigma-class PxGST) adopts the canonical fold of insect GSTs. The formation of the PxGSTσ−GTX complex is mainly driven by H-bond and hydrophobic interactions derived from the side chains of favorable residues. Of the residues composing the active site of PxGSTσ, Lys43 and Arg99 are two hot spots, first reported in the binding of GSH derivatives to GSTs. Such differences indicate the metabolism discrimination of different insect GSTs. Unfavorable interactions between the PxGSTσ active site and GTX are depicted as well. The research guides the discovery and optimization of PxGSTσ inhibitors.

KEYWORDS: *GST, GST inhibitor, molecular simulations, computational alanine scanning, site-directed mutagenesis*

INTRODUCTION

Diamondback moth (DBM), *Plutella xylostella*, is a destructive pest and causes enormous loss to global cruciferous crops.[1,2] To control this notorious pest, conventional organophosphates, carbamates, organochlorine, pyrethroid and other insecticides are often selected.[1,3] However, the rapid development of insecticide resistance significantly compromises the efficacy of insecticides and threats the current and future control of *P. xylostella*.[4,5] Currently, DBM has exhibited resistance to 91 classes of insecticides, leading to the ever increasing annual costs for DBM management. It is estimated that the costs have reached as high as $4−5 billion in recent years.[6−8] Effective strategies to slow, prevent, or even overcome insecticide resistance are urgently required.[8]

Of the mechanisms underlying insecticide resistance, enhanced metabolic activity of detoxification enzymes is an important one.[9] As a representative detoxification enzyme, insect glutathione S-transferases (GSTs, EC 2.5.1.18) compose a large and multifunctional enzyme family and primarily participate in the detoxification of xenobiotics such as insecticides.[10,11] Normally, insect GSTs are grouped into six classes: delta, epsilon, omega, sigma, theta, and zeta. All GSTs, especially delta- and epsilon-class GSTs, are best known as phase II metabolizing isozymes that conjugate reduced glutathione (GSH) to xenobiotic compounds, producing more soluble compounds that can be excreted from the cell and consequently conferring resistance toward various insecticides.[11] As reported, GSTs in particular contribute significantly to organophosphate, organochlorine, and pyrethroid resistance.[12−14] Such metabolic resistance mediated by the enhanced production of related GSTs can be alleviated or even overcome by using GST inhibitors, which help to restore the insecticide susceptibility of *P. xylostella*.[15,16]

Using a combination of insecticide and synergist is particularly effective against metabolic resistance.[17,18] As a result, it is vital to use GST inhibitors as synergists to preserve the efficacy of current and future insecticides, especially when considering the remarkable difficulty and costs associated with developing novel insecticides. However, to develop GST inhibitors as synergists, it is necessary to unravel the key interactions between GSTs and already-known GST inhibitors.

In the present research, the known GST inhibitor *S*-hexyl glutathione (GTX) is selected. We start by checking the inhibitory effects of GTX on three reported GSTs from *P. xylostella*, delta PxGST (PxGSTδ), epsilon PxGST (PxGSTε), and sigma PxGST (PxGSTσ). The most severely inhibited PxGST, PxGSTσ, is chosen as the representative of PxGSTs.

Received: July 26, 2018
Revised: September 12, 2018
Accepted: September 12, 2018
Published: September 12, 2018

DOI: 10.1021/acs.jafc.8b03967
J. Agric. Food Chem. 2018, 66, 10169−10178

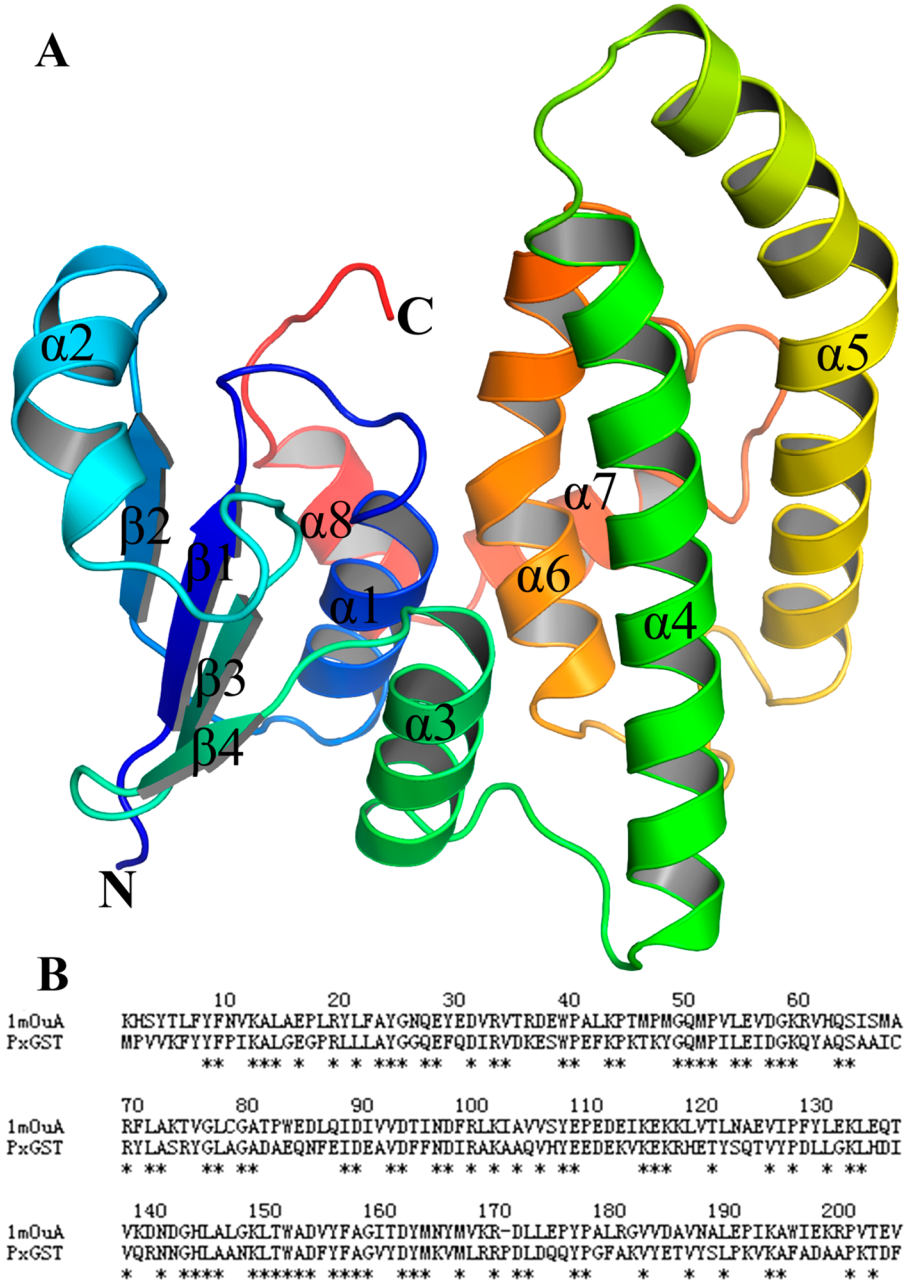

Figure 1. Structure of PxGSTσ. (A) 3D structure of PxGSTσ. N and C represent the N-terminus and the C-terminus, respectively. Helices α1−α8 and β-sheets β1−β4 are labeled as α1−α8 and β1−β4. (B) Amino acid sequence alignment of PxGSTσ and *Drosophila* sigma GST (1M0U). Conserved residues are highlighted with asterisks (*) below the letters.

Through the integrated use of homology modeling, PxGSTσ−GTX-complex construction, molecular-dynamics (MD) simulations, per-residue energy decomposition, computational alanine scanning (CAS), and site-directed mutagenesis, key interactions and key amino acids involved in the formation of the PxGSTσ−GTX complex are successfully revealed. Our results guide the further discovery and optimization of novel GST inhibitors.

MATERIALS AND METHODS

GST Inhibition by GTX. Three reported types of *P. xylostella* GSTs (PxGSTs), termed PxGSTδ, PxGSTε and PxGSTσ, were expressed and purified for inhibition studies (SI). In brief, 1 μg of recombinant PxGST protein and serial concentrations of GTX (0.16, 0.8, 4, 20, 100, 500, and 2500 μM) were premixed in 100 μL of 100 mM PBS. After being incubated at 30 °C for 10 min, the 100 μL mixture was added to 100 μL of 100 mM PBS containing 2 mM CDNB and 2 mM GSH as substrates. Using a Tecan infinite M200 Microplate Reader, absorbance changes at 340 nm were immediately monitored at 30 °C for 5 min at 1 min intervals. For each point, three replicates were performed; samples with 1 μg of denatured PxGSTs were used as negative controls. The IC_{50} values of GTX against each PxGST protein were determined via Graphpad Prism 6.0 (Graphpad Software, Inc.).

Homology Modeling and PxGSTσ−GTX-Complex Construction. After querying the PDB95 database with the amino acid sequence of PxGSTσ, the crystal structure of *Drosophila* sigma class GST (PDB ID: 1M0U, Chain A, resolution = 1.75 Å) was selected as the template for homology modeling (46% homology);[19] the 3D structure of PxGSTσ was generated and optimized by Modeler 9.10

DOI: 10.1021/acs.jafc.8b03967
J. Agric. Food Chem. 2018, 66, 10169−10178

software in accordance with our former studies.[20,21] The quality of the final PxGSTσ model was assessed by Molprobity and Profile 3D.[22−24]

The PxGSTσ−GTX complex was constructed using GOLD 5.3 software.[25] To perform molecular docking, the generated 3D model of PxGSTσ was subjected to 5000-step minimization with the bioorganic-systems force field (ff9SB) in Amber12; the 3D structure of GTX was sketched using Maestro (Schrodinger Inc.) and optimized in 2000 steps with GAFF force field in Amber12. Considering the superiority of ChemPLP in predicting binding poses, it was employed to determine the final binding model of PxGSTσ−GTX. The details of molecular docking were similar to those of our previous studies.[20,26]

Molecular-Dynamics (MD) Simulations. The Amber12 package was used to perform MD simulations of the constructed PxGSTσ−GTX complex.[27,28] The parameters and charges of GTX were optimized by GAFF and AMI-BCC methods in Amber12.[29,30] The ff9SB was used to depict PxGSTσ protein parameters.[31] Certain counterions were added to ensure the entire system was in neutral conditions (pH = 7.0). The PxGSTσ−GTX system was subjected to Amber12 for three individual 100 ns MD simulations without any restraint. MD trajectories were analyzed by the Ambertools13 package. Details of the MD simulations are shown in the Supporting Information (SI).

Binding-Free-Energy Calculation. The molecular-mechanics Poisson−Boltzmann-surface-area (MM-PBSA) method in Amber12 was utilized to calculate the binding free energy of the generated PxGSTσ−GTX complex.[32] Furthermore, the entropy contribution ($T\Delta S$) arising from changes in the translational, rational, and vibrational degrees of freedom should be taken into consideration as well. By means of the nmode program in Amber12, it was calculated using normal-mode analysis.[33] Detailed procedures were in accordance with former studies.[20,34]

Per-Residue Free-Energy Decomposition. To quantify the interactions between PxGSTσ and GTX, per-residue free-energy decomposition was performed using the MM-PBSA method incorporated in the mmpbsa.py module of Amber12. In the decomposition process, the energy contribution of each residue was calculated from three aspects: the total contribution, the side-chain contribution, and the backbone-energy contribution; each aspect was further broken into three energy items: van der Waals energy, electrostatic energy, and polar-solvation free energy. The process of energy decomposition was performed according to previous reports by our team.[20,28,35]

Computational Alanine Scanning. Computational alanine scanning (CAS) is known as an effective and reliable protocol to predict warm and hot spots.[36] For the PxGSTσ−GTX system, residues whose side chains provided >1.00 kcal/mol favorable free energy for the PxGSTσ−GTX interaction were submitted to CAS. The MM-PBSA method was further selected to calculate the binding-free-energy changes of the complexes formed by GTX and each mutant PxGSTσ protein. Details were similar to former reports.[20,26]

Site-Directed Mutagenesis and Inhibition Assay. A site-directed-mutagenesis kit (TransGen Biotech) was used to realize the site-directed mutation of PxGSTσ. Residues subjected to mutation were determined on the basis of the results of CAS; primer design and the procedure were performed according to the manufacturer's guidelines. The expression and purification of mutant PxGSTσ proteins were similar to those of wild-type PxGSTσ (SI). The inhibition-ability changes caused by site-directed mutagenesis were measured by the method detailed above in GST Inhibition by GTX.

Statistics. In the present research, the data of the inhibition assays were analyzed by Graphpad Prism 6.0 (Graphpad Software, Inc.) to obtain the corresponding IC_{50} values. The calculated IC_{50} values were further transformed to experimental binding-free-energy changes ($\Delta\Delta G_{bind\text{-}exp}$) according to eq 1.

$$\Delta\Delta G_{bind\text{-}exp} = RT \ln(IC_{50\text{-}MT}/IC_{50\text{-}WT}) \quad (1)$$

In eq 1, R and T stand for the ideal-gas constant and the temperature in Kelvin, respectively. $IC_{50\text{-}MT}$ represents the IC_{50} values of GTX and against the mutant PxGSTσ proteins, whereas $IC_{50\text{-}WT}$ is the IC_{50} value of GTX against the wild-type PxGSTσ protein.

RESULTS AND DISCUSSION

GTX Showing the Highest Inhibitory Effects on PxGSTσ. Three recombinant PxGSTs (PxGSTδ, PxGSTε, and PxGSTσ) were successfully expressed and purified (Figure S2). As revealed by inhibition tests (Figure S4), the inhibitor GTX exhibits the highest inhibition effects on the PxGSTσ protein, with the IC_{50} value being 8.83 ± 1.14 μM. The unique inhibition profiles of the PxGSTs suggest their unique substrate preferences as well as different key residues involved in the PxGST−GTX interaction. This fits with the report that different classes of PxGSTs discriminate in binding with or metabolizing xenobiotics, even though all insect GSTs adopt a highly conserved tertiary structure.[11,12] Because of the most severe inhibition by GTX, PxGSTσ was selected as the representative PxGST for following studies.

3D-Model Construction of PxGSTσ. In the present research, the 3D structure of PxGSTσ was successfully generated using the crystal structure of the *Drosophila* sigma-class GST (PDB ID: 1M0U) as the template (referred to as 1M0U). Both the Ramachandran plot (Figure S5) and the 3D profile analysis (Figure S6) suggest stereochemical rationality of the selected model.

As shown, PxGSTσ possesses the typical insect-GST fold (Figure 1A). The model is overall composed of a small, thioredoxin-like N-terminal domain (residues 1−75) and a larger, helical C-terminal domain (residues 76−204), with a wide interdomain cleft where the active site is located. To be specific, the N-terminal domain consists of a four-stranded β-sheet flanked on one side by helices α1 (residues 13−25) and α3 (residues 64−74) and on the other side by helix α2 (residues 39−49). These structural elements are arranged in a βαβαββα motif, with strand β3 being antiparallel to the other β-strands (β1, β2, and β4). Residue Pro52 at the start of strand β3 is in the *cis* conformation. Moreover, equivalent *cis* residues are conserved in all GST structures determined so far and seem to be integral to the correct formation of the catalytic site.[19,37,38] As for the C-terminal domain, it contains a bundle of five α-helices (α1, α2, α3, α4, and α5).

As mentioned above, the active site resides in a deep cleft interface of the C- and N-terminal domains (Figure 1A). It contains two subsites, termed the glutathione (GSH)-binding site (G-site) and the hydrophobic binding site (H-site). Specifically, the G-site is composed of residues that are mainly hydrophilic and polar in nature, including Tyr8, Asp35, Lys36, Trp39, Lys43, Gln50, Met51, and Arg99. With respect to the H-site, it is formed by the top sections of the α4 and α6 helices, the loop connecting the α1 helix and the β1 strand, and the C-terminus of the PxGSTσ protein. The H-site is rich in hydrophobic residues like Phe9, Pro10, Ile11, Leu14, Gly49, Pro52, Ala100, and Tyr107 (Figure S8).

Molecular-Dynamics Analysis of the PxGSTσ−GTX Complex. The PxGSTσ−GTX complex was obtained by molecular docking and analyzed by molecular-dynamics (MD) simulations. As revealed by the three individual 100 ns MD simulations, both the PxGSTσ−GTX complex and GTX converge after the equilibration phase (Figure S7) of the MD simulations. Specifically, the PxGSTσ−GTX complex achieves equilibrium at about 25 ns, with an average root-mean-square-deviation (RMSD) value of 2.67 ± 0.28 Å (Figure 2A). For the GTX molecule, it reaches equilibrium

DOI: 10.1021/acs.jafc.8b03967
J. Agric. Food Chem. 2018, 66, 10169−10178

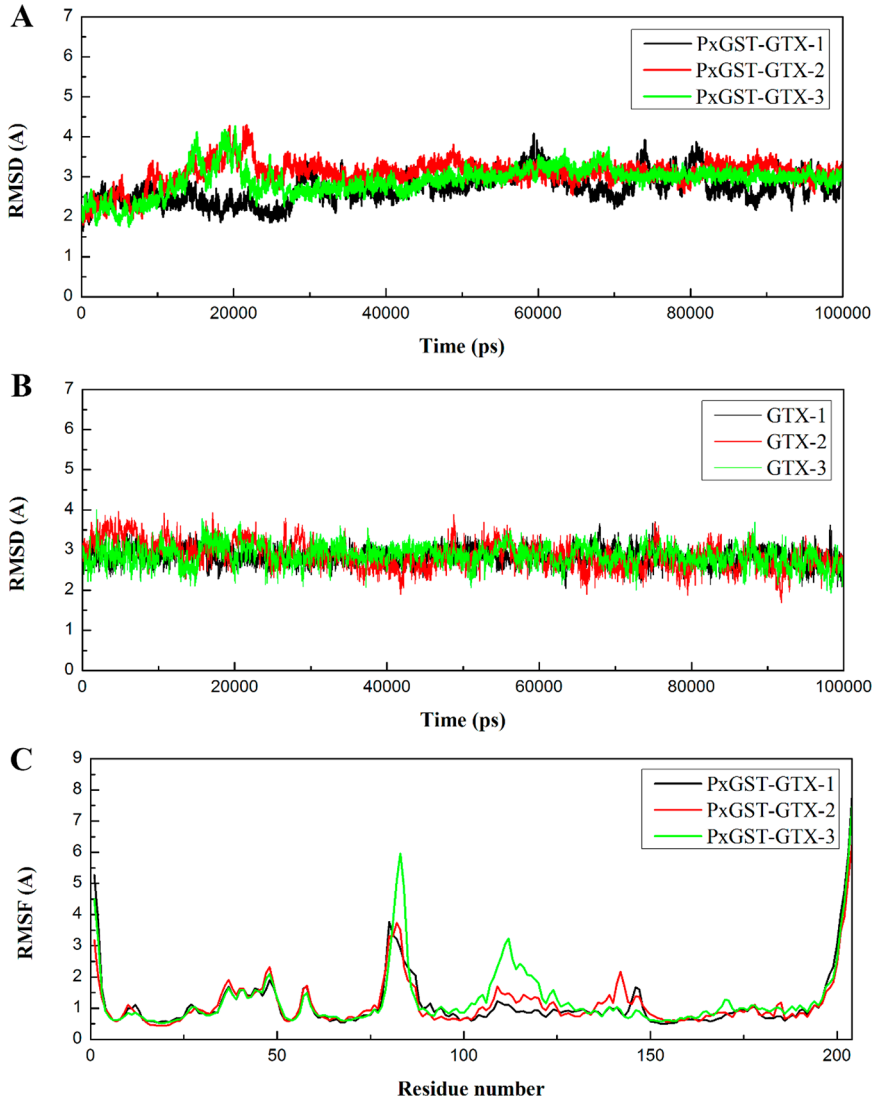

Figure 2. Molecular dynamics analysis of the PxGSTσ−GTX complex. (A) RMSD values for the PxGSTσ−GTX-complex structures monitored along three individual 100 ns molecular-dynamics simulations. (B) RMSD changes for GTX structures monitored along three individual 100 ns molecular-dynamics simulations. (C) Residue fluctuations for the PxGSTσ−GTX complex during three individual 100 ns molecular-dynamics simulations. PxGST−GTX-1, PxGST−GTX-2, and PxGST−GTX-3 are three repetitions of the RMSD and RMSF values for the PxGSTσ−GTX complex. GTX-1, GTX-2, and GTX-3 are three repetitions of RMSD values for GTX.

earlier than the PxGSTσ−GTX complex. In Figure 2B, GTX becomes stable right after 10 ns, with an RMSD of 2.85 ± 0.18 Å.

Considering the secondary-structural elements in the PxGSTσ model (Figure 1A), it is necessary to unravel the flexibility and local-motion characters on the binding of GTX. On the basis of MD simulations, root-mean-square fluctuation (RMSF) is adopted to evaluate the local flexibility of the PxGSTσ−GTX complex. As shown (Figure 2C), helix regions are more rigid than loop regions; this is particularly evident when comparing the short loops between α3 and α4, α4 and α5, and α5 and α6. The effects caused by the flexible C-terminal and N-terminal tails are negligible to the GTX-binding interface of the PxGSTσ−GTX complex because of their distances from the active sites. Actually, in the course of the 100 ns MD simulations, residues associated with the PxGSTσ−GTX interaction, including Tyr8, Phe9, Ile11, Leu14, Trp39, Lys43, Met51, Arg99, Ala103, and Tyr107 all presented little RMSF fluctuation (Figures 2C and 3). All the data indicate stability of the PxGSTσ−GTX complex we generated.

Binding-Mode Analysis of the PxGSTσ−GTX Complex. According to the MD representative conformation of the PxGSTσ−GTX complex (Figure 3), the GTX molecule sits tightly inside the active pocket of PxGSTσ, with its GSH moiety binding to the G-site and the *S*-hexyl moiety occupying the H-site (Figure S8).

Powerful hydrogen-bond (H-bond) nets are detected between the glutathione from GTX and the G-site of PxGSTσ. The oxygen atom from the top carboxyl terminal of GTX forms two H-bonds with the NZ atom from the Lys43 side chain and the NE1 atom from the Trp39 side chain (Figure 3 and Table S3), with averaged N−O distances of 2.87 and 2.92 Å, respectively. The oxygen atom from the bottom carboxyl terminal of GTX interacts with NH1 and NH2 from the Arg99 side chain through salt-bridges, with N−O distances 2.7 and 2.8 Å (Figure 3). Two hydrogen bonds are also detected between the carbonyl of the GTX glutamyl and the −OH from

DOI: 10.1021/acs.jafc.8b03967
J. Agric. Food Chem. 2018, 66, 10169−10178

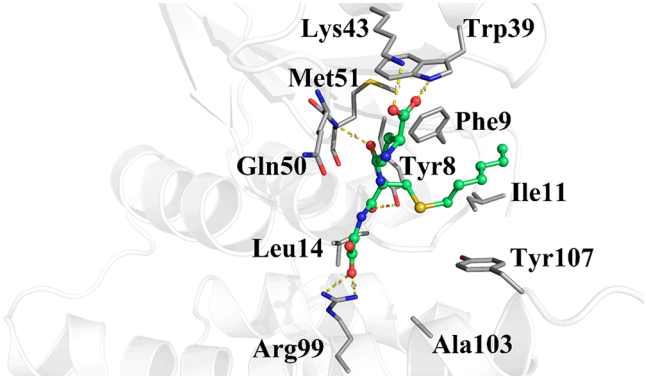

Figure 3. Key interactions and H-bond patterns at the active site observed during MD simulations of GTX. GTX is shown as a stick-and-sphere model. Green, C; red, O; blue, N; gold, S. Involved residues are shown as sticks. Gray, C; red, O; blue, N; gold, S. H-bonds are shown as yellow dashed lines.

the Tyr8 side chain (averaged O−O distance of 2.75 Å) and between the carbonyl of the GTX cysteinyl and the N atom from the Met51 backbone (N−O distance of 2.97 Å). Not only that, other interactions, including a polar interaction (GTX and Gln50), a positively charged interaction (GTX and Lys36), and a negatively charged interaction (GTX and Asp35), are determined between GTX and PxGSTσ as well. According to cluster analysis of the MD trajectories (Table S3), the H-bonds formed with GTX and Lys43, Tyr8, and Arg99 exhibit fairly high occupancy rates (83.66, 76.94, and 73.80%). Such high H-bond-occupancy rates suggest the stability and actual existence of these H-bonds. For the H-bonds derived from Met51 (55.14%) and Trp39 (46.96%), their existence is not supposed to be that stable, because of their relatively lower occupancy rates during the 100 ns MD simulations. In particular, the H-bond formed between GTX and Trp39 has an occupancy rate lower than 50% (Table S3).

On the basis of the results of conformational superimposition (Figure 4), little structural deviation is checked between the MD representative structure of the PxGSTσ−GTX complex and the template we chose for homology modeling (PDB ID: 1M0U); key interactions depicted in 1M0U are present in the PxGSTσ−GTX complex as well. For example, Trp39 and Met51 from PxGSTσ are equivalent to Trp85 and Met97 from 1M0U, and they all form H-bond interactions with the corresponding ligands. Such high interaction similarity suggests that the representative PxGSTσ−GTX conformation revealed by MD simulations approximates to the data provided by 1M0U.

Binding-Free-Energy Calculation. To calculate the theoretical binding free energy ($\Delta G_{\text{bind-cal}}$) of the generated PxGSTσ−GTX complex, an MM-PBSA approach is employed. As revealed by Table 1, electrostatic interaction (ΔE_{ELE} = −101.10 kcal/mol) contributes the most to the formation and stability of the PxGSTσ−GTX complex, this corresponds to the powerful H-bond nets between GTX and PxGSTσ. Other elements, including hydrophobic interactions (ΔE_{VDW} = −30.01 kcal/mol) and nonpolar parts of the solvation free energy (ΔE_{SURF} = −27.26 kcal/mol), provide favorable contributions to the binding of GTX. As for the polar part of the solvation free energy (ΔE_{EGB} = 103.91 kcal/mol), it is negative to the PxGSTσ−GTX interaction. After the introduction of conformational entropy ($-T\Delta S$ = 25.98 kcal/mol), the absolute binding free energy ($\Delta G_{\text{bind-cal}}$) of the PxGSTσ−GTX complex is calculated to be −6.67 kcal/mol. The experimental binding free energy ($\Delta G_{\text{bind-exp}}$ = −5.49 kcal/mol) is also determined on the basis of the inhibitory effects (IC_{50} = 8.83 ± 1.14 μM) of GTX against PxGSTσ. The acceptable difference between $\Delta G_{\text{bind-cal}}$ and $\Delta G_{\text{bind-exp}}$ suggests reliability of the MD representative structure of the PxGSTσ−GTX complex.

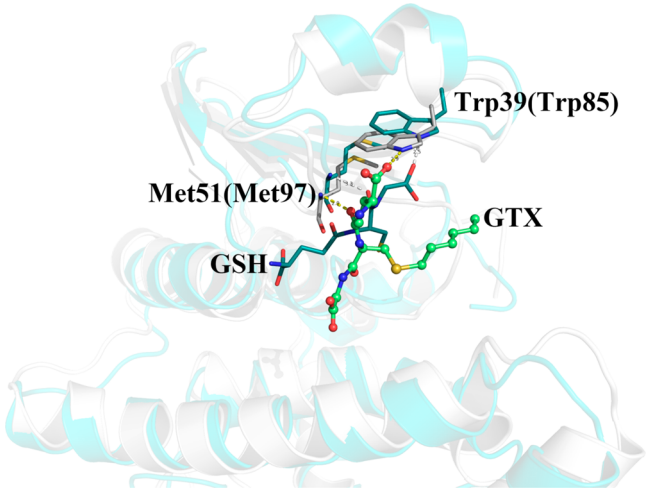

Figure 4. Superimposition of the PxGSTσ−GTX complex and the *Drosophila* sigma GST−GSH complex. The model of the *Drosophila* sigma GST−GSH complex we used is its crystal structure (PDB ID: 1M0U). GTX is presented with a stick-and-sphere model. Key residues and GSH are presented with stick models. Yellow and gray dashed lines represent the H-bond interactions derived from the PxGSTσ−GTX and *Drosophila* sigma GST−GSH complexes.

Per-Residue Free-Energy Decomposition. The MM-PBSA method is used to quantify and decompose the energy contribution of each residue from PxGSTσ. As shown (Figure 5 and Table 2), 11 residues (Tyr8, Phe9, Ile11, Leu14, Trp39, Lys43, Gln50, Met51, Arg99, Ala103, and Tyr107) contribute over 0.50 kcal/mol of the total free energy (T_{TOT}) to the binding of GTX, of which Trp39 (−2.79 kcal/mol), Lys43 (−5.60 kcal/mol), and Arg99 (−8.50 kcal/mol) are particularly highlighted because of their high total energy contributions. In Table 2, it can be seen that Lys43 and Arg99 provide remarkably unfavorable polar solvation energies (T_{EPB}), possibly because of their exposure to solvent. However, this unfavorable energy is neutralized by the electrostatic energies (T_{ELE}) derived from their side chains (Table 2), further indicating the powerful and stable H-bond nets formed between GTX and Lys43 and between GTX and Arg99. Trp39 and Tyr8 interact similarly with GTX; their energy contributions mainly derive from H-bond interactions (Trp39 T_{ELE} = −5.28 kcal/mol, Tyr8 T_{ELE} = −5.78 kcal/mol). However, the total energy contributions of the two residues are quite different (−2.79 kcal/mol for Trp39, −1.74 kcal/mol for Tyr8). Such a difference can be generally attributed to the lower van der Waals energy (T_{VDW}) and greater T_{EPB} provided by Tyr8 (Table 2). For Phe9, Gln50, and Tyr107, they exhibit similar interaction spectra with considerable T_{VDW} (above 1.80 kcal/mol) and limited T_{ELE}. Meanwhile, their T_{EPB} losses are tiny because of their relatively large distances from the solvent.

Besides the residues providing beyond 1.00 kcal/mol to T_{TOT}, mentioned above, Met51 contributing −0.77 kcal/mol to T_{TOT} is also noteworthy. As shown in the superimposed

DOI: 10.1021/acs.jafc.8b03967
J. Agric. Food Chem. 2018, 66, 10169−10178

Table 1. Calculated and Experimental Binding Free Energies for the PxGSTσ−GTX Complex[a]

energy items	ΔE_{ELE}	ΔE_{VDW}	ΔE_{EPB}	ΔE_{SURF}	ΔG_{gas}	ΔG_{sol}	$-T\Delta S_{TOT}$	$\Delta G_{bind\text{-}cal}$[b]	$\Delta G_{bind\text{-}cal}$[c]	$\Delta G_{bind\text{-}exp}$
energy values	−101.10 (1.10)	−30.01 (0.38)	103.91 (0.88)	−5.46 (0.03)	−131.10 (0.99)	98.46 (0.88)	25.98 (1.00)	−32.65 (0.35)	−6.67 (0.65)	−5.49

[a]All values are given in kilocalories per mole (kcal/mol), with corresponding standard errors of the mean in parentheses. [b]Predictions of binding free energy without considering the entropy effect. [c]Predictions of binding energy considering the entropy effect.

figure (Figure 4), Met51 of PxGSTσ−GTX corresponds to Met97 of the template 1M0U. In 1M0U, Met97 is reported to be a key residue by forming a H-bond interaction with GSH.[19] However, in the PxGSTσ−GTX complex we constructed, the total energy contribution (T_{TOT}) of Met51 does not even exceed 1.00 kcal/mol, probably because of the unfavorable electrostatic energy provided by the Met51 backbone (B_{ELE} = 1.38 kcal/mol), despite the −1.25 kcal/mol T_{VDW} and −1.69 kcal/mol S_{ELE} derived from its side chain. Moreover, the highly unfavorable B_{ELE} of Met51 may be attributable to polar interactions between GTX and neighboring residue Gln50 (Figure S8). Specifically, the polar interaction provided by Gln50 had significant negative effects on the H-bond stability formed between GTX and the Met51 backbone. Consequently, to optimize GTX for better PxGST inhibitors, the polar interaction with Gln50 should be avoided.

CAS-Based Site-Directed Mutagenesis. Computational alanine scanning (CAS) is regarded as a reliable avenue for recognizing residues key to protein−protein or protein−ligand interactions.[36] In the current research, five residues (Tyr8, Phe9, Trp39, Lys43, and Arg99) whose side chains provide >1.00 kcal/mol favorable energy (Figure 5B) were individually mutated into Ala. The theoretical binding-free-energy change ($\Delta\Delta G_{bind\text{-}cal}$) of each mutant PxGSTσ is calculated and listed in Table 3. According to the criteria of hot spots ($\Delta\Delta G_{bind} \geq$ 4.00 kcal/mol), warm spots (2.00 kcal/mol ≤ $\Delta\Delta G_{bind} \leq$ 4.00 kcal/mol) and null spots ($\Delta\Delta G_{bind}$ < 2.00 kcal/mol),[36] three residues, Phe9, Lys43, and Arg99, are theoretically predicted to be hot spots in the PxGSTσ−GTX interaction.

To verify the results of CAS, five corresponding mutant PxGSTσ proteins (PxGSTσY8A, PxGSTσF9A, PxGSTσW39A, PxGSTσK43A, and PxGSTσR99A) are produced and subjected to inhibition tests. As reported, GTX is a known inhibitor of PxGSTσ protein, with its IC_{50} value calculated as 8.83 ± 1.14 μM. However, its inhibitory activity was suppressed to varying degrees as a result of the individual replacement of Tyr8, Phe9, Trp39, Lys43, and Arg99 with Ala (Figure 6). Compared with the IC_{50} of wild-type PxGSTσ (8.83 ± 1.14 μM), that of PxGSTσK43A exhibits the largest increase (78.32 ± 13.25 μM). It is consequently taken as the most unfavorable one to the binding of GTX. Mutations of Arg99 and Phe9 cause significant decreases in the inhibitory effects of GTX on PxGSTσ activity as well, with IC_{50} values increasing to 50.31 ± 9.64 μM for PxGSTσR99A and 36.80 ± 8.93 μM for PxGSTσF9A. As for the rest of the residues, Tyr8 and Trp39, their mutation results relatively weak, negative effects on the affinity between GTX and PxGSTσ; corresponding IC_{50} values for PxGSTσY8A and PxGSTσW39A are 17.93 ± 2.61 and 16.91 ± 5.41 μM, respectively.

To compare the results of CAS, the IC_{50} values of the five mutant PxGSTσ proteins were transformed to experimental binding free energies ($\Delta\Delta G_{bind\text{-}exp}$). As shown in Table 3, the results of the CAS and inhibition tests are in qualitative agreement, and differences between corresponding values of $\Delta\Delta G_{bind\text{-}exp}$ and $\Delta\Delta G_{bind\text{-}cal}$ are within the limits as well. Moreover, the $\Delta\Delta G_{bind\text{-}exp}$ and $\Delta\Delta G_{bind\text{-}cal}$ values listed in Table 3 have a good linear correlation, for which R^2 reaches 0.94 (Figure S9). Of the five mutant proteins, only PxGSTσK43A and PxGSTσR99A possess $\Delta\Delta G_{bind\text{-}cal}$ (−7.57 and −5.10 kcal/mol) and $\Delta\Delta G_{bind\text{-}exp}$ (−5.50 and −4.38 kcal/mol) of more than 4.00 kcal/mol simultaneously. As a result, it could be concluded that Lys43 and Arg99 are two hot spots (key residues) involved in the interaction between PxGSTσ

DOI: 10.1021/acs.jafc.8b03967
J. Agric. Food Chem. 2018, 66, 10169−10178

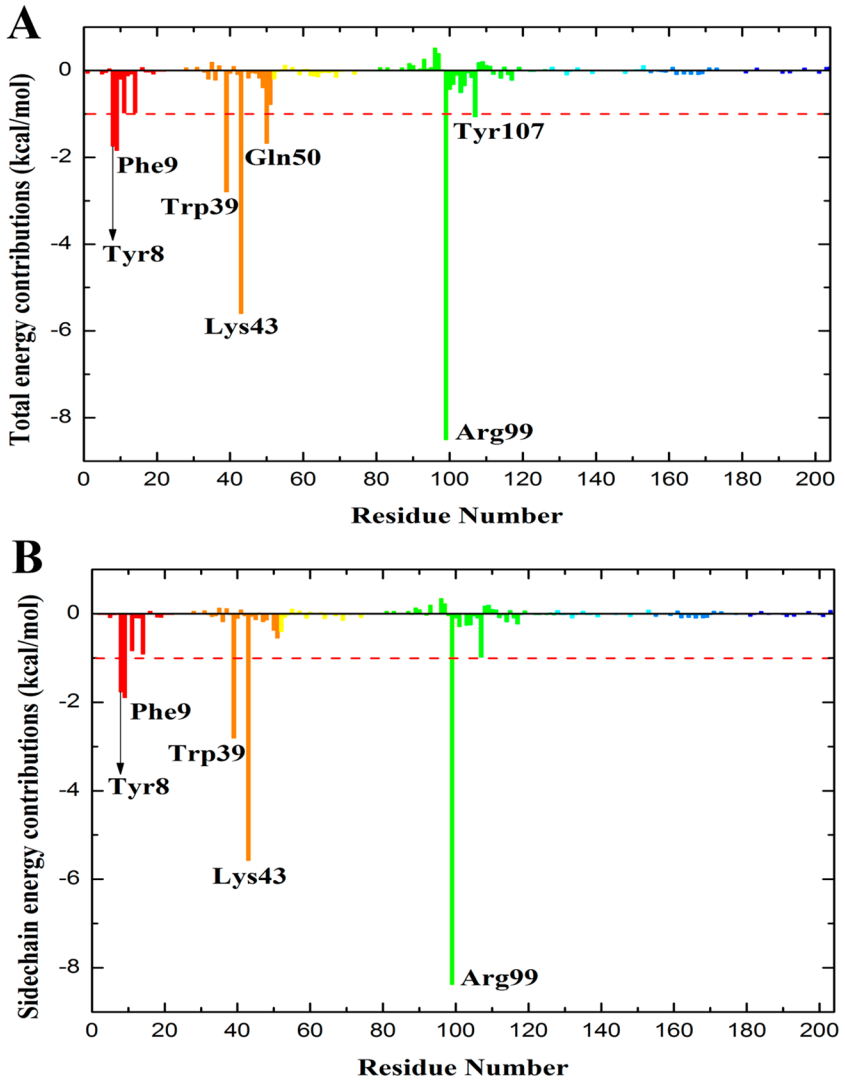

Figure 5. Residue−ligand-interaction spectra of the PxGSTσ−GTX complex based on the MM-PBSA method. The *X*-axis denotes the residue number of PxGSTσ, the *Y*-axis denotes (A) total-interaction free-energy and (B) side-chain free-energy contributions of each residue. Residues contributing above 1.00 kcal/mol binding free energy are marked.

Table 2. Results of Per-Residue Free-Energy Decomposition[a]

residue	S_{VDW}	B_{VDW}	T_{VDW}	S_{ELE}	B_{ELE}	T_{ELE}	S_{EPB}	B_{EPB}	T_{EPB}	S_{TOT}	B_{TOT}	T_{TOT}
Tyr8	−0.47	−0.056	−0.52	−5.46	−0.32	−5.78	4.16	0.40	4.56	−1.76	0.024	−1.74
Phe9	−2.22	−0.18	−2.40	−1.02	0.24	−0.78	1.35	−0.012	1.34	−1.89	0.052	−1.84
Trp39	−1.043	−0.048	−1.09	−5.55	0.27	−5.28	3.79	−0.22	3.58	−2.8	0.009	−2.79
Lys43	0.20	−0.035	0.16	−27.69	0.32	−27.37	21.92	−0.31	21.61	−5.57	−0.023	−5.60
Gln50	−1.27	−0.62	−1.89	1.72	−2.04	−0.32	−0.82	1.35	0.53	−0.37	−1.31	−1.67
Arg99	0.58	−0.06	0.51	−44.97	0.51	−44.46	36.02	−0.58	35.45	−8.37	−0.13	−8.50
Tyr107	−1.72	−0.087	−1.80	0.27	0.023	0.29	0.47	−0.019	0.45	−0.98	−0.083	−1.06
Ile11	−0.89	−0.096	−0.98	−1.23	1.48	0.25	1.29	−1.52	−0.24	0.83	−0.14	−0.97
Leu14	−0.82	−0.13	−0.95	−2.28	1.28	−1.00	2.19	−1.21	0.98	−0.91	−0.06	−0.96
Met51	−0.382	−0.86	−1.25	−1.69	1.38	−0.32	1.53	−0.74	0.76	0.544	−0.23	−0.77
Ala103	−0.24	−0.13	−0.37	−0.23	−1.63	−1.86	0.22	1.51	1.73	−0.25	−0.25	−0.50

[a]Energies are shown as contributions from van der Waals energy (VDW), electrostatic energy (ELE), polar solvation energy (EPB), and total energy (TOT) of the side-chain atoms (*S*), the backbone atoms (*B*), and the sum of them (*T*). All values are given in kilocalories per mole (kcal/mol).

and GTX. It is noteworthy that these two residues are first reported to be key residues involved in the interactions between insect GSTs and their corresponding ligands.[19,37] For the protein PxGSTσF9A, its $\Delta\Delta G_{bind\text{-}exp}$ (−3.60 kcal/mol) and $\Delta\Delta G_{bind\text{-}cal}$ (−4.06 kcal/mol) caused by changing Phe9 into Ala are close to 4.00 kcal/mol. Therefore, Phe9 is taken to be a warm spot, which refers to residues potentially key to the binding of GTX.

DOI: 10.1021/acs.jafc.8b03967
J. Agric. Food Chem. 2018, 66, 10169−10178

Table 3. Theoretical and Experimental $\Delta\Delta G_{bind}$[a] Values for the Mutant PxGSTσ−GTX Complex

protein[b]	Y8A	F9A	W39A	K43A	R99A
$\Delta\Delta G_{bind\text{-}cal}$	−1.91	−4.10	−2.45	−7.57	−5.10
$\Delta\Delta G_{bind\text{-}exp}$[c]	−1.78	−3.60	−1.64	−5.50	−4.38

[a]All values are given in kcal/mol. [b]Y8A, F9A, W39A, K43A, and R99A are abbreviations for PxGSTσY8A, PxGSTσF9A, PxGSTσW39A, PxGSTσK43A, and PxGSTσR99A, respectively. [c]The binding-free-energy difference ($\Delta\Delta G_{bind}$) between the mutant and wild-type PxGSTσ−GTX complexes is defined as $\Delta\Delta G_{bind} = RT \ln(IC_{50\text{-}MT}/IC_{50\text{-}WT})$, where R is the ideal gas constant, and T is the temperature in Kelvin.

What should be mentioned is that the key interaction residues are not necessarily in good correlation with the corresponding impacts on IC_{50} and $\Delta\Delta G_{bind}$ (including $\Delta\Delta G_{bind\text{-}cal}$ and $\Delta\Delta G_{bind\text{-}exp}$). Take Arg99 and Phe9 for example: although their total interaction-energy contributions (−8.50 kcal/mol for Arg99, −1.84 kcal/mol for Phe9) are significantly different, their impacts on the IC_{50} and $\Delta\Delta G_{bind}$ changes are similar. This can be explained. As revealed, the relatively high total energy contribution (T_{TOT}) of Arg99 can be largely attributed to the salt-bridge formed between GTX and Arg99. From Table 2, it can be found that the total electrostatic energy (T_{ELE}) of Arg99 (−44.46 kcal/mol) is much higher than that of Phe9 (−0.78 kcal/mol). However, because of the closer distances to solvent, Arg99 also contributes more total polar-solvation energy (T_{EPB} = 35.45 kcal/mol) than Phe9 (T_{EPB} = 1.34 kcal/mol). Such highly negative contributions can greatly neutralize the energy differences between Arg99 and Phe9. As a result, the $\Delta\Delta G_{bind}$ differences caused by the individual mutations of Arg99 and Phe9 are not as significant as expected.

As a derivative of GSH, GTX is somewhat different from GSH in its interaction with insect GST. As reported, Tyr54 and Trp85 in 1M0U (corresponding to Tyr8 and Trp39 in PxGSTσ, respectively) provide important H-bond interactions for the binding of GSH,[19] whereas in the PxGSTσ−GTX complex we constructed, Tyr8 and Trp39 are categorized into null spots because of the small energy changes ($\Delta\Delta G_{bind\text{-}exp}$) caused by mutations. Such differences may be associated with the metabolic discrimination of different GSTs.

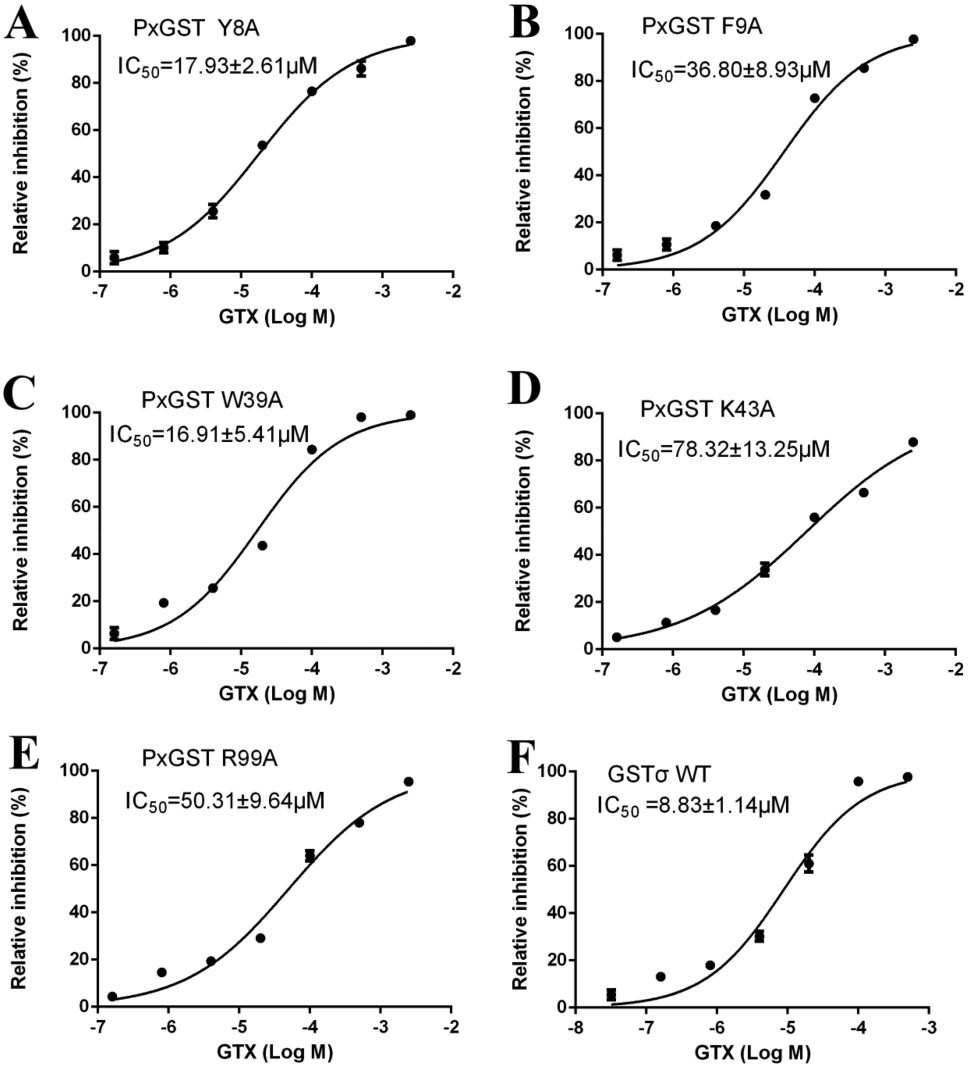

Figure 6. Inhibitory effects of GTX against wild-type and mutant PxGSTσ proteins. PxGST Y8A, PxGST F9A, PxGST W39A, PxGST K43A and PxGST R99A represent the five mutant PxGSTσ proteins whose Tyr8, Phe9, Trp39, Lys43, and Arg99 residues are individually replaced with Ala. GSTσ WT represents the wild-type PxGSTσ.

DOI: 10.1021/acs.jafc.8b03967
J. Agric. Food Chem. 2018, 66, 10169−10178

To conclude, the interaction modes between PxGSTσ and GTX (a known GST inhibitor) are revealed through the integrated application of molecular simulations and biological tests. GTX sits tightly in the PxGSTσ active site, which is composed of two subsites, the G-site (rich in hydrophilic and polar residues) and the H-site (characterized by hydrophobic residues). As revealed, the formation and stability of the PxGSTσ–GTX complex are mainly driven by the H-bond interactions provided by GSH–protein contacts and hydrophobic interactions derived from *S*-hexyl–protein contacts. Our results of per-residue free-energy decomposition verify this statement. Residues key to the binding of GTX are determined as well. The two hot spots (Lys43 and Arg99) we discovered have not ever been reported in other GST–GTX interactions, whereas for some residues categorized as null spots in our research (like Tyr8 and Trp39), their equivalent residues in other insect GTSs, such as Tyr54 and Trp85 in 1M0U, are distinguished by significant H-bond interactions. The differences in the residues involved in the PxGSTσ–GTX interaction may contribute to the metabolism discrimination of GSTs.

Insect GSTs are of great importance to the metabolic resistance of many insecticides, including organophosphate, organochlorine, and pyrethroid, leaving chances for the management or alleviation of field resistance by using GST inhibitors as synergists. Through the revelation of the PxGSTσ–GTX interaction, the present research provides the basis for the discovery and optimization of novel PxGSTσ inhibitors.

■ ASSOCIATED CONTENT

Supporting Information

The Supporting Information is available free of charge on the ACS Publications website at DOI: 10.1021/acs.jafc.8b03967.

Methods for protein expression and purification, enzyme-kinetics detection, and molecular-dynamics simulations; supplement to the enzyme-kinetics results; gene and amino acids sequences; SDS-PAGE analysis of wild-type and mutant proteins; enzyme kinetics; inhibitory effects of GTX; Ramachandran plot; profile 3D score; RMSD values; 2D interaction diagram; linear correlation between theoretical and experimental binding-free-energy changes; classification of insect GSTs; primers for site-directed mutagenesis; and H-bond interactions (PDF)

■ AUTHOR INFORMATION

Corresponding Author

*E-mail: yalinzh@nwsuaf.edu.cn.

ORCID

Jiyuan Liu: 0000-0002-3524-2064

Author Contributions

⊥J.Y.L., Y.F.L., and Z.T. contributed equally to this work. J.Y.L. and Y.L.Z. conceived the project. J.Y.L. and Y.L.Z. designed the experiment. J.Y.L., Y.F.L., Z.T., H.S., X.E.C., and S.L.Z., performed the experiments and prepared the manuscript. Y.L.Z. supervised the study and contributed reagents and materials. All authors contributed to data analysis.

Funding

The research was supported by the Fundamental Research Funds for the Central Universities (2452018008), the Sci-Tech Planning Project of Yangling Demonstration Zone (2018NY-02), the National Natural Science Foundation of China (21503272), the Special Fund for the Public Interest (Agriculture) by the Ministry of Science and Technology and the Ministry of Agriculture of China (200903052), and the "13115" Sci-Tech Innovation Project of Shaanxi Province (2007ZDKG-14).

Notes

The authors declare no competing financial interest.

■ REFERENCES

(1) Li, Z.; Feng, X.; Liu, S. S.; You, M.; Furlong, M. J. Biology, ecology, and management of the diamondback moth in China. *Annu. Rev. Entomol.* **2016**, *61*, 277–296.

(2) Juric, I.; Salzburger, W.; Balmer, O. Spread and global population structure of the diamondback moth *Plutella xylostella* (Lepidoptera: Plutellidae) and its larval parasitoids *Diadegma semiclausum* and *Diadegma fenestrale* (Hymenoptera: Ichneumonidae) based on mtDNA. *Bull. Entomol. Res.* **2017**, *107*, 155–164.

(3) Sarfraz, M.; Keddie, B. Conserving the efficacy of insecticides against *Plutella xylostella* (L.) (Lep., Plutellidae). *J. Appl. Entomol.* **2005**, *129*, 149–157.

(4) Zhou, L.; Huang, J.; Xu, H. Monitoring resistance of field populations of diamondback moth *Plutella xylostella* L.(Lepidoptera: Yponomeutidae) to five insecticides in South China: a ten-year case study. *Crop Prot.* **2011**, *30*, 272–278.

(5) Khaliq, A.; Attique, M.; Sayyed, A. Evidence for resistance to pyrethroids and organophosphates in *Plutella xylostella* (Lepidoptera: Plutellidae) from Pakistan. *Bull. Entomol. Res.* **2007**, *97*, 191–200.

(6) Santos, V.; De Siqueira, H.; Da Silva, J.; De Farias, M. Insecticide resistance in populations of the diamondback moth, *Plutella xylostella* (L.) (Lepidoptera: Plutellidae), from the state of Pernambuco, Brazil. *Neotrop. Entomol.* **2011**, *40*, 264–270.

(7) Zalucki, M. P.; Shabbir, A.; Silva, R.; Adamson, D.; Liu, S. S.; Furlong, M. J. Estimating the economic cost of one of the world's major insect pests, *Plutella xylostella* (Lepidoptera: Plutellidae): just how long is a piece of string? *J. Econ. Entomol.* **2012**, *105*, 1115–1129.

(8) Furlong, M. J.; Wright, D. J.; Dosdall, L. M. Diamondback moth ecology and management: problems, progress, and prospects. *Annu. Rev. Entomol.* **2013**, *58*, 517–541.

(9) Sparks, T. C.; Nauen, R. IRAC: Mode of action classification and insecticide resistance management. *Pestic. Biochem. Physiol.* **2015**, *121*, 122–128.

(10) Huang, H. S.; Hu, N. T.; Yao, Y. E.; Wu, C. Y.; Chiang, S. W.; Sun, C. N. Molecular cloning and heterologous expression of a glutathione S-transferase involved in insecticide resistance from the diamondback moth, *Plutella xylostella*. *Insect Biochem. Mol. Biol.* **1998**, *28*, 651–658.

(11) Pavlidi, N.; Vontas, J.; Van Leeuwen, T. The role of glutathione S-transferases (GSTs) in insecticide resistance in crop pests and disease vectors. *Curr. Opin. Insect Sci.* **2018**, *27*, 97–102.

(12) Ketterman, A. J.; Saisawang, C.; Wongsantichon, J. Insect glutathione transferases. *Drug Metab. Rev.* **2011**, *43*, 253–265.

(13) Enayati, A. A.; Ranson, H.; Hemingway, J. Insect glutathione transferases and insecticide resistance. *Insect Mol. Biol.* **2005**, *14*, 3–8.

(14) Hsu, J. C.; Lin, Y. Y.; Chang, C. C.; Hua, K. H.; Chen, M. J. M.; Huang, L. H.; Chen, C. Y. Discovery of organophosphate resistance-related genes associated with well-known resistance mechanisms of *Plutella xylostella* (L.) (Lepidoptera: Plutellidae) by RNA-Seq. *J. Econ. Entomol.* **2016**, *109*, 1378–1386.

(15) Smagghe, G. Synergism of diacylhydrazine insecticides with metyrapone and diethylmaleate. *J. Appl. Entomol.* **2004**, *128*, 465–468.

(16) Wang, Z.; Zhao, Z.; Abou-Zaid, M. M.; Arnason, J. T.; Liu, R.; Walshe-Roussel, B.; Waye, A.; Liu, S.; Saleem, A.; Cáceres, L. A.; et al. Inhibition of insect glutathione s-transferase (GST) by conifer extracts. *Arch. Insect Biochem. Physiol.* **2014**, *87*, 234–249.

(17) Wang, J. J.; Wei, D.; Dou, W.; Hu, F.; Liu, W. F.; Wang, J. J. Toxicities and synergistic effects of several insecticides against the oriental fruit fly (Diptera: Tephritidae). *J. Econ. Entomol.* **2013**, *106*, 970−978.
(18) Wang, S. P.; Hu, X. X.; Meng, Q. W.; Muhammad, S. A.; Chen, R. R.; Li, F.; Li, G. Q. The involvement of several enzymes in methanol detoxification in *Drosophila melanogaster* adults. *Comp. Biochem. Physiol., Part B: Biochem. Mol. Biol.* **2013**, *166*, 7−14.
(19) Agianian, B.; Tucker, P. A.; Schouten, A.; Leonard, K.; Bullard, B.; Gros, P. Structure of a *Drosophila* sigma class glutathione S-transferase reveals a novel active site topography suited for lipid peroxidation products. *J. Mol. Biol.* **2003**, *326*, 151−165.
(20) Tian, Z.; Liu, J.; Zhang, Y. Key residues involved in the interaction between *Cydia pomonella* pheromone binding protein 1 (CpomPBP1) and Codlemone. *J. Agric. Food Chem.* **2016**, *64*, 7994−8001.
(21) Liu, J.; Yang, X.; Zhang, Y. Characterization of a lambda-cyhalothrin metabolizing glutathione S-transferase CpGSTd1 from *Cydia pomonella* (L.). *Appl. Microbiol. Biotechnol.* **2014**, *98*, 8947−8962.
(22) Šali, A.; Blundell, T. L. Comparative protein modelling by satisfaction of spatial restraints. *J. Mol. Biol.* **1993**, *234*, 779−815.
(23) Chen, V. B.; Arendall, W. B.; Headd, J. J.; Keedy, D. A.; Immormino, R. M.; Kapral, G. J.; Murray, L. W.; Richardson, J. S.; Richardson, D. C. MolProbity: all-atom structure validation for macromolecular crystallography. *Acta Crystallogr., Sect. D: Biol. Crystallogr.* **2010**, *66*, 12−21.
(24) Bowie, J. U.; Luthy, R.; Eisenberg, D. A method to identify protein sequences that fold into a known three-dimensional structure. *Science* **1991**, *253*, 164−170.
(25) Jones, G.; Willett, P.; Glen, R. C.; Leach, A. R.; Taylor, R. Development and validation of a genetic algorithm for flexible docking. *J. Mol. Biol.* **1997**, *267*, 727−748.
(26) Liu, J.; Tian, Z.; Zhang, Y. Structure-based discovery of potentially active semiochemicals for *Cydia pomonella* (L.). *Sci. Rep.* **2016**, *6*, 34600.
(27) Tian, Z.; Liu, J.; Zhang, Y. Structural insights into *Cydia pomonella* pheromone binding protein 2 mediated prediction of potentially active semiochemicals. *Sci. Rep.* **2016**, *6*, 22336.
(28) Liu, J.; Tian, Z.; Zhou, N.; Liu, X.; Liao, C.; Lei, B.; Li, J.; Zhang, S.; Chen, H. Targeting the apoptotic Mcl-1-PUMA interface with a dual-acting compound. *Oncotarget* **2017**, *8*, 54236−54242.
(29) Jakalian, A.; Jack, D. B.; Bayly, C. I. Fast, efficient generation of high-quality atomic charges. AM1-BCC model: II. Parameterization and validation. *J. Comput. Chem.* **2002**, *23*, 1623−1641.
(30) Wang, J.; Wolf, R. M.; Caldwell, J. W.; Kollman, P. A.; Case, D. A. Development and testing of a general amber force field. *J. Comput. Chem.* **2004**, *25*, 1157−1174.
(31) Hummer, G.; Rasaiah, J. C.; Noworyta, J. P. Water conduction through the hydrophobic channel of a carbon nanotube. *Nature* **2001**, *414*, 188.
(32) Hou, T.; Wang, J.; Li, Y.; Wang, W. Assessing the performance of the molecular mechanics/Poisson Boltzmann surface area and molecular mechanics/generalized Born surface area methods. II. The accuracy of ranking poses generated from docking. *J. Comput. Chem.* **2011**, *32*, 866−877.
(33) Kottalam, J.; Case, D. Langevin modes of macromolecules: applications to crambin and DNA hexamers. *Biopolymers* **1990**, *29*, 1409−1421.
(34) Liu, J. Y.; Chen, X. E.; Zhang, Y. L. Insights into the key interactions between human protein phosphatase 5 and cantharidin using molecular dynamics and site-directed mutagenesis bioassays. *Sci. Rep.* **2015**, *5*, 12359.
(35) Yang, X. Q.; Liu, J. Y.; Li, X. C.; Chen, M. H.; Zhang, Y. L. Key amino acid associated with acephate detoxification by *Cydia pomonella* carboxylesterase based on molecular dynamics with alanine scanning and site-directed mutagenesis. *J. Chem. Inf. Model.* **2014**, *54*, 1356−1370.
(36) Moreira, I. S.; Fernandes, P. A.; Ramos, M. J. Computational alanine scanning mutagenesis-an improved methodological approach. *J. Comput. Chem.* **2007**, *28*, 644−654.
(37) Chen, L.; Hall, P. R.; Zhou, X. E.; Ranson, H.; Hemingway, J.; Meehan, E. J. Structure of an insect δ-class glutathione S-transferase from a DDT-resistant strain of the malaria vector Anopheles gambiae. *Acta Crystallogr., Sect. D: Biol. Crystallogr.* **2003**, *59*, 2211−2217.
(38) Armstrong, R. N. Structure, catalytic mechanism, and evolution of the glutathione transferases. *Chem. Res. Toxicol.* **1997**, *10*, 2−18.

DOI: 10.1021/acs.jafc.8b03967
J. Agric. Food Chem. 2018, 66, 10169−10178